



## Flow behavior prediction at free-fibrous interface

Jinliang Kang, Moran Wang\*

Department of Engineering Mechanics, Tsinghua University, Beijing, 100084, China

### ARTICLE INFO

#### Keywords:

Brinkman double-layer model  
Free-fibrous interface  
Interfacial transport  
Fibrous structure  
Pore-scale modeling

### ABSTRACT

The interfacial transport phenomena in free space and fibrous structure coupling regions appear widely in energy and environmental systems. At the same time, the flow behavior at interfaces fails to be accurately predicted by the previous models, which were essentially based on the granular porous structures. This work examines the validity of the recently proposed Brinkman double-layer model by pore-scale simulations at the interface between free space and 3D fibrous porous structures. The geometrical characteristics, including anisotropy and tortuosity of fibers, and the flow conditions have been comprehensively studied utilizing a random generation growth (RGG) method. The results indicate that the Brinkman double-layer model can capture the fluid dynamics at the free-fibrous interface robustly and effectively, providing a powerful tool for predicting flow behavior at free-porous interfaces.

### 1. Introduction

Complex fibrous structures have recently gained widespread applications across diverse fields, owing to their remarkable physical properties [1,2]. Among the numerous challenges encountered in these applications, a crucial issue arises concerning fluid flow interactions between free space and neighboring fibrous porous structures. This phenomenon finds extensive use in various scenarios, including composite material fabrications [3], underground contaminant transport [4], food industry [5], fuel cells [6,7], heat exchangers [8], paper production [9], and biological contexts [10]. Understanding the interfacial transport dynamics between the fibrous network and the clean channel is of paramount importance, as this interfacial transport significantly impacts the flow behavior on both sides. Nevertheless, the inherent complexity and variable anisotropy of these fibrous structures present a formidable yet essential fundamental problem.

The interfacial transport phenomena in free-fibrous coupled systems can be comprehended at three levels. At the microscopic level, fluid flow throughout the domain is governed by the Navier–Stokes equation (or the Stokes equation for the creeping flow). However, due to the intricate geometry of the porous media, conducting microscale simulations across the entire domain becomes computationally prohibitive. As a result, macroscopic level models are necessary for most practical applications. In order to bridge the gap between the microscale and macroscale levels, upscaling techniques are required to derive mesoscopic descriptions, in which the porous media is treated as a heterogeneous new phase. Among the upscaling methods available, two commonly used approaches are the volume-average method [11,12] and the asymptotic expansion method [13,14].

In the literature, macroscale models designed for free-porous systems often lack the specificity to accommodate diverse porous structures. These models frequently rely on the simplifying assumption of isotropic granular structures. These models can be broadly categorized into one-domain [12,15] and two-domain approaches [16,17]. The latter two-domain approaches are favored for their enhanced simplicity, achieved by integrating interface conditions to link governing equations within two distinct flow regions. This simplicity renders them particularly attractive for various practical applications. Based on the governing equations and interface conditions, they can be further sorted into various categories, such as the Stokes–Darcy models, Stokes–Brinkman models, velocity-continuous models, and velocity-jump models. The first Stokes–Darcy model was introduced by Beavers and Joseph [18] and Saffman [19] with a velocity-jump interface condition. This model is the most famous and widely-used model due to its simplicity. However, the applications of this model have met more and more limitations as it suffers from severe dependence on the posterior model parameter  $\alpha$  and ignorance of the existence of a transition layer near the interface, which is the most critical feature in this free-porous coupled flow system. After identifying a transition layer near the free-porous interface instead of abrupt velocity change [20,21], Bars and Worster [22] proposed a Stokes–Darcy model incorporating a velocity-continuum interface condition by utilizing the Stokes equation in the transition layer. The incompatibility of the first-order Darcy term with the second-order Stokes equation in such Stokes–Darcy models led to the development of the Stokes–Brinkman model, which includes an additional second-order Brinkman term [23].

\* Corresponding author.

E-mail address: [mrwang@tsinghua.edu.cn](mailto:mrwang@tsinghua.edu.cn) (M. Wang).

The first Stokes–Brinkman model was proposed by Neale and Nader [24], imposing continuity in both velocity and shear stress at the free-porous interface. Subsequently, the Stokes–Brinkman model underwent modification to include velocity-continuum but stress-jump interface conditions, as undertaken by Ochoa-Tapia and Whitaker [25] and other researchers [26]. However, despite ongoing research advocating for continuous velocity and discontinuous shear stress [27], these models frequently necessitate empirical determination of at least one model parameter or the solution of complex auxiliary problems [13, 28], potentially complicating practical applications. Furthermore, the Brinkman equation has been deemed unsuitable for describing transition flow within the interface layer by numerous studies [29,30]. In response to these challenges, Kang and Wang [31] introduced a Brinkman double-layer (BDL) model featuring a unique double-layer structure and a stress-jump interface condition. They recommended using an alternative governing equation instead of the Brinkman equation for modeling flow in the outer layer. They proposed a straightforward linear expression for the model parameter denoted as  $\gamma$ . While the BDL model demonstrated remarkable accuracy and robustness when applied to complex granular porous structures, its suitability for fibrous structures warrants further investigation.

In contrast to the commonly assumed isotropic granular porous structures, fibrous porous structures exhibit a notable diversity in anisotropy and connectivity. A significant portion of fibrous structures displays pronounced anisotropy, resulting in substantial variations in flow resistance along different directions. Furthermore, fibrous structures can possess stronger connectivity due to the high aspect ratio of fibers compared to granular structures with the same porosity, leading to higher permeability. Previous investigations into various physical properties, such as conductivity and diffusivity [7,32], have demonstrated that fibrous porous structures manifest distinct characteristics compared to traditional granular structures. Consequently, interfacial transport dynamics in free-fibrous coupled flow systems likely exhibit considerable deviations from granular structures in response to the morphology of individual fibers and the fiber arrangement. Several studies have examined commonly used models like the B-J model [18], the Stokes–Brinkman model [24], and the O-W model [25] in the context of fibrous porous structures, and none of these models yielded satisfactory results: These models do not predict the flow behavior in the interface region correctly, and their performance can vary dramatically in structures with different porosity values. Furthermore, all these models contain one posterior model parameter that is difficult to decide in real applications [33,34]. While a limited number of experimental and numerical studies have explored interfacial flow transfer in free-fibrous coupled systems, these investigations often involve a narrow range of fibrous media types with simple geometries. The majority of these studies have focused on 2D fibrous structures that are either aligned parallel or perpendicular to the flow direction [35–37], featuring strong periodicity and regularity. These geometric limitations may compromise the generalizability of flow patterns, particularly given that the porosity of these structures is typically constrained to values above 0.5. Additionally, wavy patterns in velocity profiles arising from structural regularity can impede the precise quantification of flow characteristics.

Numerous investigations have explored the influence of fiber morphology on the permeability of fibrous porous media. These studies could serve as a valuable foundation for inspiring further inquiries into the impact of structural anisotropy on interfacial transport phenomena within free-fibrous coupled flow systems [38,39]. While prior research has primarily focused on three categories of fibrous structures: layered, neatly aligned, and nearly isotropic configurations [40–42], the integration of these intricate fibrous networks into the free-fibrous coupled flow system can broaden the spectrum of structures under investigation. This expansion might provide valuable insights into the influence of structural anisotropy on interfacial transport phenomena.

In summary, a significant research gap exists in quantitative investigations into macroscale modeling of the interfacial transport within the free-fibrous coupled flow system, with particular emphasis on complex 3D fibrous structures. A critical assessment of existing macroscale models is still needed, alongside a comprehensive exploration of the effects of structural anisotropy.

In this work, we strive to contribute valuable insights into the applications of the Brinkman double-layer model in predicting flow behavior in free-fibrous coupled flow systems (Fig. 1), shedding light on the geometrical influences and advancing understanding of the interfacial transport dynamics. To achieve this, distinct types of fibrous structures with varying anisotropy and porosity are generated by a stochastic–statistic method. Pore-scale simulations are conducted in the free-fibrous domain comprising these diverse structures, and the interfacial flow dynamics are analyzed using several quantitative parameters. Ultimately, we thoroughly examine the validity and robustness of the Brinkman double-layer (BDL) model for the free-fibrous systems.

The organization of this paper is as follows: In Section 2, we provide a concise overview of the previously proposed Brinkman double-layer (BDL) model and the four quantitative parameters. A comparison is conducted between the BDL model and existing experimental data. Section 3 is dedicated to outlining the methodology employed in this study. We introduce the random generation growth(RGG) and pore-scale simulation methods, elucidating the processes involved. In Section 4, we present the diverse morphology of the generated fibrous structures and compare the BDL model with pore-scale simulation results. The validity of the BDL model is addressed by additional in-depth discussions of the influence of flow parameters. Finally, the conclusions are provided in Section 5.

## 2. Brinkman double-layer model

Recently, a Brinkman double-layer (BDL) model has been proposed for the free-porous coupled flow system. This model was proposed under the common Stokes flow assumption, and it has displayed remarkable efficacy when applied to complex 3D granular porous structures [31]. This model incorporates a velocity-continuity boundary condition, a stress-jump boundary condition, and a novel double-layer structure near the free-porous interface. Within these two interface layers, distinct governing equations are utilized to seamlessly connect the Stokes flow in the clean channel and Darcy flow in the bulk porous medium. In this framework, velocity and shear stress are assumed to be continuous in between.

### 2.1. Mathematical description

The stress-jump condition contains a model parameter  $\gamma$ , which was introduced by a linear assumption of the shear force  $f(u_s, K, \varepsilon) = \mu \cdot \gamma(\varepsilon) \cdot \frac{u_s}{\sqrt{K}}$ , in which  $u_s$  stands for the average fluid velocity at the free-porous interface,  $K$  stands for the permeability,  $\mu$  stands for the fluid viscosity, and  $\varepsilon$  stands for the porosity. A semi-empirical linear expression for  $\gamma$  was proposed for granular porous structures as  $\gamma = 2\varepsilon$ . This straightforward expression for the model parameter gains great advantages compared to other models since the model parameter can be easily calculated priorly, and no fittings or auxiliary equations are needed.

One key issue in applying this model to anisotropy porous media is how to deal with the permeability tensor. Since it is almost impossible to measure all the components of this permeability tensor in irregular porous structures, we suggest using the two scalar permeability values along the flow direction and perpendicular to the flow direction(also perpendicular to the free-porous interface) denoted as  $K_{\parallel}$  and  $K_{\perp}$ , respectively. The  $K_{\parallel}$  is used to characterize the stream-wise structural damping resistance and the corresponding viscous resistance, appearing in the governing equations. The  $K_{\perp}$ , on the other hand, represents

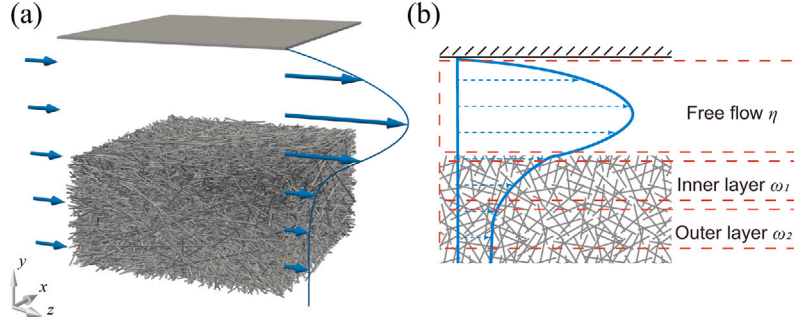


Fig. 1. Schematic diagram of (a) the free-fibrous coupled flow system and (b) the Brinkman double layer (BDL) model.

the ability of the porous structure to transfer mass and momentum vertically and decides how deep the two interface layers penetrate the porous medium. These two permeability values are much easier to measure in applications. The complete mathematical description of this BDL model for anisotropic porous media is as follows.

At the upper solid wall

$$\mathbf{u} = 0, \quad \text{at } y = H, \quad (1)$$

Flow in the clean channel

$$0 = -\nabla \langle p_\beta \rangle_\eta^\beta + \mu_\beta \nabla^2 \langle \mathbf{u}_\beta \rangle_\eta, \quad 0 < y < H. \quad (2)$$

At the free-porous interface

$$\langle \mathbf{u}_\beta \rangle_\eta = \langle \mathbf{u}_\beta \rangle_{\omega_1}, \quad \text{at } y = 0. \quad (3)$$

$$\frac{\partial \langle \mathbf{u}_\beta \rangle_\eta}{\partial y} - \frac{1}{\varepsilon} \frac{\partial \langle \mathbf{u}_\beta \rangle_{\omega_1}}{\partial y} = \gamma(1 - \varepsilon) \frac{\mathbf{u}_s}{\sqrt{K_{\parallel}}}, \quad \text{at } y = 0. \quad (4)$$

Flow in the inner Brinkman layer

$$0 = -\nabla \langle p_\beta \rangle_{\omega_1}^\beta + \frac{\mu_\beta}{\varepsilon} \nabla^2 \langle \mathbf{u}_\beta \rangle_{\omega_1} - \frac{\mu_\beta}{K_{\parallel}} \langle \mathbf{u}_\beta \rangle_{\omega_1}. \quad (5)$$

At the interface between inner and outer Brinkman layer

$$\langle \mathbf{u}_\beta \rangle_{\omega_1} = \langle \mathbf{u}_\beta \rangle_{\omega_2}, \quad \text{at } y = -\sqrt{K_{\perp}}. \quad (6)$$

$$\frac{\partial \langle \mathbf{u}_\beta \rangle_{\omega_1}}{\partial y} = \frac{\partial \langle \mathbf{u}_\beta \rangle_{\omega_2}}{\partial y}, \quad \text{at } y = -\sqrt{K_{\perp}}. \quad (7)$$

Flow in the outer Brinkman layer

$$0 = -\nabla \langle p_\beta \rangle_{\omega_2}^\beta + \frac{\mu_\beta}{\varepsilon \sqrt{K_{\parallel}}} \nabla \langle \mathbf{u}_\beta \rangle_{\omega_2} \cdot \frac{\mathbf{u}_\beta}{|\mathbf{u}_\beta|} - \frac{\mu_\beta}{K_{\parallel}} \langle \mathbf{u}_\beta \rangle_{\omega_2}. \quad (8)$$

Flow in the bulk of porous medium

$$\langle \mathbf{u}_\beta \rangle_{\omega_2} \rightarrow \mathbf{u}_{\text{Darcy}}, \quad \text{when } y \rightarrow -\infty. \quad (9)$$

In the above equations, we follow some commonly adopted notations:  $H$  stands for the channel height,  $\beta$  refers to the fluid phase (in both subscripts and superscripts),  $\eta$  refers to the clean channel,  $\omega$  refers to the porous media (subscripts 1 and 2 stands for different layers of porous media), and triangular brackets stands for the averaged value of certain fields. More detailed definitions can be found in many previous works employing the volume-averaging technique [25,31]. When  $K_{\parallel} = K_{\perp}$ , the above model is then simplified to the BDL model for isotropic porous media [31].

General analytical solutions can be derived from solving the governing equations of the three distinct flow regions. Once all boundary conditions, the porosity and permeability values specific to the structure in question, and the linear expression  $\gamma = 2\varepsilon$  are taken into account, it is feasible to compute the precise velocity distribution

along the  $y$ -axis. This calculated velocity profile can be compared with simulation or experimental results for validation and assessment.

In this study, we will examine the BDL model with the linear equation  $\gamma = 2\varepsilon$  in free-fibrous coupled flow systems comprising complex 3D fibrous structures by the following four parameters:

- $u_s$ : slip velocity: the planar average velocity at the free-fibrous interface. It is calculated by averaging the pore-scale velocity along the  $x$ - $z$  plane at the free-fibrous interface. The magnitude of this velocity characterizes the intensity of the mass and momentum transfer at the free-porous interface and is strongly related to the structure morphology near the interface.
- $\delta$ : interface layer thickness. This interface layer is defined by the magnitude of the macroscale filtration velocity  $u$ , which should meet the following inequality inside this layer:

$$u_s - u \leq 0.95 (u_s - u_{\text{Darcy}}), \quad (10)$$

where  $u_{\text{Darcy}}$  is the Darcy filtration velocity and  $u_s$  is the slip velocity. To determine the thickness, we start by calculating the fluid velocity at the boundary of the interface layer using the equation provided. Subsequently, we identify the two nodes whose velocities bracket this calculated value. The precise position of the edge of the interface layer is then determined by interpolating the fluid velocities of neighboring nodes. The thickness of this interface layer, which is the major feature of this coupled flow system, represents the penetration depth of the outer flow impact and is closely related to the transverse mass and momentum transport ability of the porous matrix.

- $\tau_{\text{channel}}$ : shear stress at the free-fibrous interface calculated from the side of the clean channel. This parameter is calculated by  $\tau_{\text{channel}} = \mu \partial \langle \mathbf{u}_\beta \rangle_\eta / \partial y|_{y=0^+}$ , and characterizes the force on the outer flow exerted by the porous matrix.
- $\tau_{\text{dif}}$ : shear stress difference between two sides at the free-fibrous interface defined by  $\tau_{\text{dif}} = \tau_{\text{channel}} - \tau_{\text{porous}}$ . This parameter characterizes the force balance at the free-porous interface, which is the deeper cause behind this interfacial transport phenomenon. This parameter is the most important one, reflecting whether a model can correctly capture the underlying dynamics of the flow phenomenon.

These four parameters can be calculated from the cross-sectional velocity profile and provide more quantitative and comprehensive characterizations of the interfacial transport phenomena than a single velocity profile. More detailed descriptions of these parameters can be found elsewhere [31].

## 2.2. Experimental validation

To validate the BDL model, we first compare it with two of the few existing experimental studies utilizing fibrous structures as porous

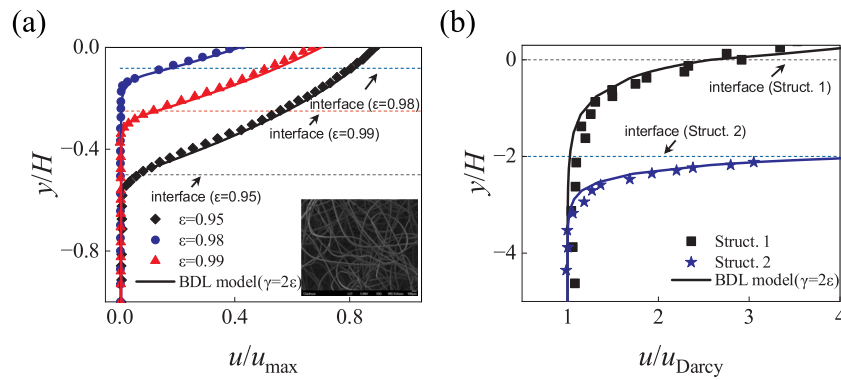


Fig. 2. (a) Performance of the BDL model in random fibrous porous media compared to experiments by Wu and Mirbod [43]. The subfigure illustrates the morphology of the fibrous structure utilized in the experiment. (b) Performance of the BDL model in regular fibrous porous media compared to experiments by Rosenzweig and Shavit [44]. Different symbols stand for different pieces of porous media, and the solid lines represent the BDL model.

media. Both studies placed a clean channel on top of a piece of porous media to form the free-fiber coupled flow system and used the particle image velocimetry (PIV) technique to measure the fluid velocity. In the first study conducted by Wu and Mirbod [43], the porous media was made of polyester and silk had random fibrous structures, and three pieces of these porous media with different porosity values were tested under pressure-driven flow conditions. In these three experiments, the total height of the channel remains consistent, and the thickness of the porous media varies, leading to different interface locations marked by dash lines and arrows in Fig. 2(a). The morphology of the fibers is shown in the subfigure. In the second experiment [44], regular arrays of vertical square columns presenting Sierpinski patterns were used as porous media. Two structures with the same permeability and porosity value of 0.79 but different thicknesses were tested in gravity-driven flow conditions with an oblique flume. The results of these two experiments are shown in Fig. 2. The  $y$ -axis is nondimensionalized by the channel height  $H$ , while the fluid velocity is nondimensionalized by the maximum velocity in the pressure-driven flow and the Darcy velocity in the gravity-driven flow, respectively.

In the comparisons, we mainly focused on the velocity profiles in the interface region, which is the prominent feature of such free-fibrous coupled flow systems. The results demonstrate commendable alignment between experiments and the BDL model in both random and regular fibrous porous structures.

Further validation of the BDL model with experimental data has met some formidable challenges, primarily due to the limitations of available observation and measurement techniques. Historically, most prior experiments relied on porous structures composed of neatly aligned pillars, essentially 2D granular structures with wavy velocity distribution patterns. The porosity values of the fibrous structures in experiments are close to 1 to provide a clear vision for velocity measurement techniques like the PIV, imposing further restrictions.

Given the above constraints posed by the available structures and observational techniques in experimental studies, there is a pressing need for further numerical investigations, particularly concerning diverse fiber morphology, anisotropy, and a wider range of porosity values and flow conditions. Sequentially, we conduct pore-scale simulations within free-fibrous coupled flow systems, encompassing various types of fibrous structures. We aim to thoroughly assess the Brinkman double-layer (BDL) model by quantitatively analyzing its performance through the four key parameters and provide a more comprehensive understanding of its applicability under diverse conditions and structures.

### 3. Methods

This section outlines the methodologies utilized for conducting pore-scale flow simulations within the free-fibrous coupled systems. We

focus on two critical aspects: techniques for generating complex 3D fibrous porous structures and the direct numerical simulation method for fluid flows at the pore scale.

#### 3.1. Fibrous porous structure generation

To create complex 3D fibrous porous structures, we utilize a stochastic method known as the Random Generation Growth (RGG) method [45], which emulates the natural growth process of real-life fibers. The generation process commences by randomly selecting seeding points within the spatial domain. The exact density of the seeds in each case is random, but the expected value is pre-defined. Following this, two orientation angles, denoted as  $\theta$  (polar angle) and  $\phi$  (azimuthal angle), are randomly assigned to each seeding point.

The sequential generation process consists of numerous discrete growth time steps, during which each fiber extends towards both ends with a specified probability by a unit length. More specifically, every fiber is assigned a random number within the range of 0 to 1 in each time step. The fiber is extended if this randomly generated number is smaller than a designated probability. Different fibers are allowed to overlap to maintain growth orientations, which will not make much difference to the morphology of the entire fiber network. This growth process continues iteratively until the overall porosity of the structure reaches a predefined threshold.

This stochastic approach enables the random growth of fibers and serves as a foundation for incorporating multiple tunable parameters. These parameters can be adjusted to further manipulate the fibers' morphology, including orientation tendencies, length distributions, curvature, cluster formation, and more. Consequently, this method allows for the generation of complex 3D fibrous porous structures with varying degrees of anisotropy and tailored characteristics.

Through meticulous parameter manipulation within this method, we successfully generated five unique types of fibrous porous media. Each type comprises numerous structures characterized by varying porosity and permeability values. To ensure the validity of our simulations, the domain size of these structures is selected to satisfy Brinkman's screening length criterion, a well-established standard widely used in prior research [39,42]. The grid resolution is set to  $400 \times 160 \times 400$  for the porous medium and  $400 \times 200 \times 400$  for the whole flow system containing the clean channel. In all of these structures, the diameter of the fibers was consistently set to 4 lattice units.

#### 3.2. Pore-scale simulation method

For the incompressible fluid flow in the free-fibrous coupled systems, the governing equations, i.e., the Navier–Stokes (N–S) equation

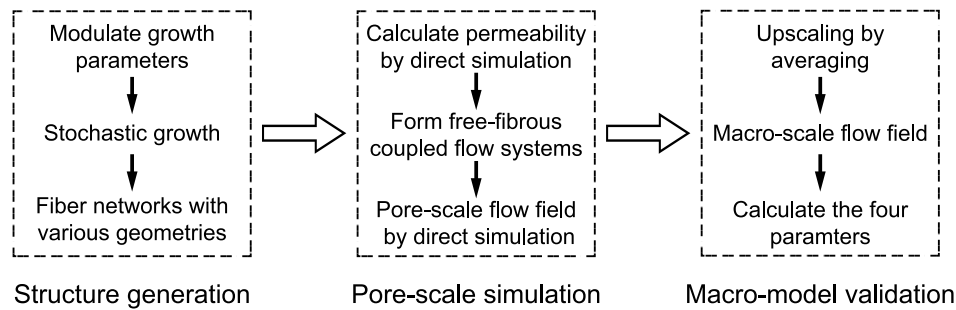


Fig. 3. Flowchart of the organization of the methods utilized in the present work.

and the continuity equation, are as follows:

$$\frac{\partial \mathbf{u}}{\partial t} + (\mathbf{u} \cdot \nabla) \mathbf{u} = -\frac{1}{\rho} \nabla p + \nu \nabla^2 \mathbf{u}, \quad (11)$$

$$\nabla \cdot \mathbf{u} = 0.$$

The N-S equation can be fully recovered from the following lattice Boltzmann equation (LBE) by Chapman–Enskog expansion:

$$f_i(\mathbf{x} + \mathbf{c}_i \Delta t, t + \Delta t) = f_i(\mathbf{x}, t) + \Omega_i(\mathbf{x}, t). \quad (12)$$

With this equation, the time and velocity space are discretized in the lattice Boltzmann method (LBM). Due to the locality of the LBE, the LBM is highly amenable to parallel computing, rendering it suitable for large-scale simulations [46,47]. Furthermore, the highly efficient implementations of boundary conditions in LBM make it well-suited for modeling flow in porous structures [48–50]. In the present work, single-relaxation-time (SRT) and multiple-relaxation-time(MRT) schemes are employed with a D3Q19 velocity set. The relaxation time of the SRT scheme has been set to one, and the multiple relaxation times of the MRT scheme are subject to specific constraints to maintain consistent truncation errors across different viscosity values [51]. The fluid–solid interfaces in this system are treated as no-slip boundaries by the bounce-back approach. The pressure boundaries at the entrance and exit of the channel are implemented using the Zou & He approach [52–54]. This LB solver has been successfully used in our previous studies [7,55–57].

The methods are organized as follows: stochastic methods are used to generate realistic, complex 3D fibrous porous structures, which are then combined with a clean channel to form free-fibrous coupled flow systems. Within these systems, pore-scale simulations are conducted using LBM. To determine the permeability of these fibrous structures, we performed additional LBM simulations incorporating periodic boundary conditions. Then, the macro-scale flow field is obtained from the pore-scale simulation results by upscaling technique (average along the x-z plane) and is then utilized to calculate the four key parameters, which are subsequently compared with the results obtained from the model(Fig. 3). Throughout our study, gravitational effects have been disregarded.

It is worth pointing out that the stream-wise permeability (denoted as  $K_{||}$ ) is measured along the same direction as the flow in the free-fibrous coupled systems(z-axis). In porous structures with strong anisotropy, additional pore-scale simulations are performed to measure the transverse permeability (denoted as  $K_{\perp}$ ) along the vertical direction, and this permeability is only used for deciding the Brinkman layer thickness in the BDL model. Unless otherwise specified, the permeability  $K$  referred to in the following text and figures exclusively denotes the stream-wise permeability.

This combination of realistic fibrous structures and pore-scale flow simulations enables us to study a wide range of scenarios, effectively capture the intricate and varied flow dynamics in these systems, and conduct comprehensive examinations of the macro models.

## 4. Results and discussion

This section presents the results of the five types of fibrous structures generated by the RGG method: two types of isotropic fibrous structures, two types of anisotropic fibrous structures, and one type of tortuous fibrous structures. The morphology of these structures is illustrated and further characterized by their permeability patterns. The results of the four parameters are summarized for each type of fibrous structure, and the predictions of the BDL model are compared with the results of the pore-scale simulation. Moreover, we engage in a discussion that delves into the influence of flow conditions beyond structural morphology to emphasize the validity of the BDL model.

### 4.1. Isotropic fibrous structures

Initially, we focused on generating isotropic fibrous porous structures, including randomly grown straight fibers with varying and uniform lengths. The first type consists of naturally grown straight fibers produced using the RGG method (as shown in Fig. 4a). To ensure isotropy, we distributed the azimuthal angle  $\phi$  uniformly within the range of  $[0, 2\pi]$ , while for the polar angle  $\theta$ ,  $\cos \theta$  was evenly distributed within the interval  $[-1, 1]$ . This approach prevents fiber aggregation along the z-axis and maintains isotropy in the flow direction. For these naturally grown fibrous structures, 6 different values have been set for the maximum fiber length:  $l_{\max} = 40, 80, 120, 160, 200, 240$ . For each value of  $l_{\max}$ , ten distinct structures with porosity values ranging from 0.2 to 0.99 have been generated. By manipulating fiber density, the fiber length distribution shows similar Gaussian patterns for each structure (Fig. 4e).

The second type of isotropic fibrous structure comprises randomly piled cylinders with the same aspect ratio (AR). The generation processes of these structures follow the same seeding rules as the complete RGG method, but the lengths of the fibers are restricted to the same value. We also applied the same rules described above to select the two orientation angles  $\theta$  and  $\phi$  to avoid anisotropy. The aspect ratios were set to 10, 20, 30, 40, 50, and 60, ensuring that the mean fiber lengths of these structures were roughly equivalent to those of the naturally grown isotropic fibers. Fig. 4(b) presents one example of this type of isotropic fibrous structure.

The permeability values of the two types of isotropic fibrous structures are plotted against porosity in Fig. 4(c) and (d). The permeability values have been nondimensionalized with the square of the radius of the fibers following conventions by previous studies. The dash and solid lines represent the naturally grown fibers and randomly piled cylinders, respectively, with different symbol sizes and shades representing distinct fiber lengths. Both types of fibrous structures show identical inverse “S” patterns, which can be divided into three stages:

- Pre-linear stage ( $0.2 < \epsilon < 0.4$ ): In this stage, the increasing speed of permeability decreases with increasing porosity.
- Linear stage ( $0.4 < \epsilon < 0.8$ ): As porosity values increase within this range, the permeability shows a proportional response.

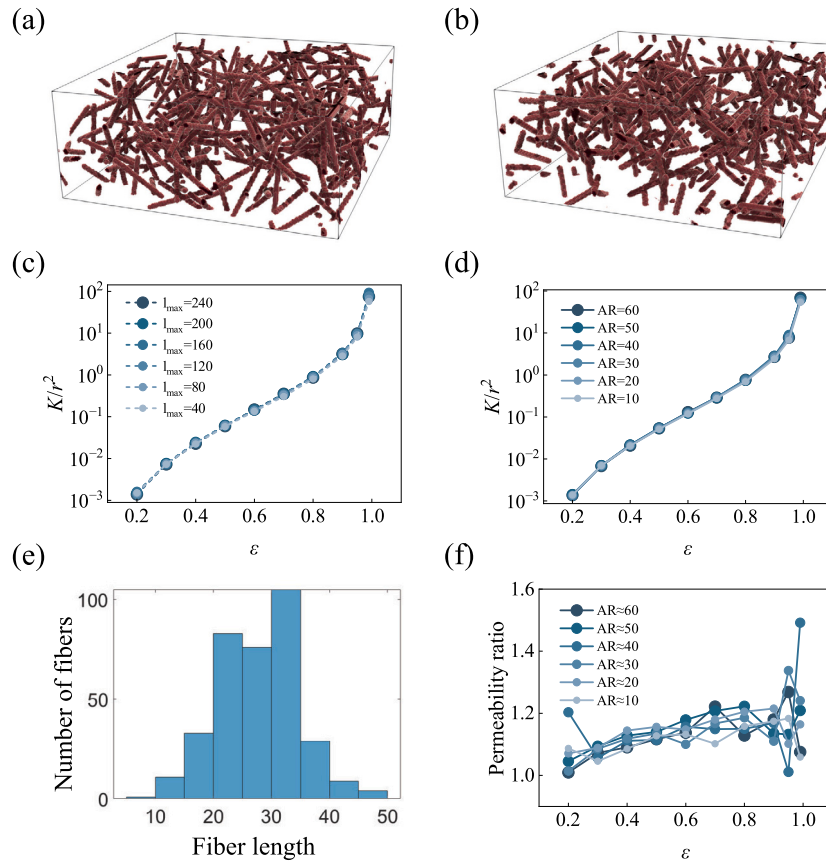


**Fig. 4.** Schematic diagram of the naturally grown straight fibers (a) and randomly piled cylinders (b) having the same porosity( $\epsilon = 0.95$ ). (c) and (d) show the relationship between permeability and porosity for the naturally grown straight fibers and randomly piled cylinders, respectively.  $r$  stands for the radius of the fibers. (e) The corresponding fiber length distribution of the structure illustrated in (a). (f) The permeability ratio of the two types of isotropic fibrous structures(naturally grown straight fibers over randomly piled cylinders) versus porosity.

- Post-linear stage ( $0.8 < \epsilon < 1.0$ ): In this stage, the increasing speed of permeability intensifies as porosity approaches its maximum value.

It is worth pointing out that the fiber length appears to have minimal influence on permeability for both types of isotropic structures.

Since the average fiber length is approximately half of the maximum fiber length for the naturally grown fibers, the two types of fibrous structures represented by symbols with the same size and color have roughly equivalent average fiber lengths. Accordingly, we compare the permeability of these two types of structures with roughly the same mean fiber length and plot the permeability ratio (naturally grown fibers over randomly piled cylinders) against porosity in Fig. 4(f). Generally, naturally grown fibrous structures exhibit higher permeability than randomly piled cylinders by an average of 14%. This difference becomes more pronounced as porosity increases. This result highlights the systematic variation in fiber morphology between these two types of structures, underscoring the importance of considering the fiber length distribution pattern when analyzing flow problems involving fibrous structures, especially sparse ones.

Results of the four parameters in free-fibrous coupled flow systems comprising the naturally grown straight fibers generated above are shown in Fig. 5. Results of fibrous structures with the porosity of 0.99 are neglected because the porosity value is too high, leading to over-scattering in the interface layer thickness. Blue squares of distinct shades and sizes represent fibers with different lengths, and the red solid line represents predictions of the BDL model.

The slip velocity is nondimensionalized by the average velocity in the Poiseuille flow with the same pressure gradient and channel height.

Concurrently,  $\sqrt{K}$  is nondimensionalized by the channel height  $H$ . Despite the striking differences in porosity and permeability among these fibrous structures, the slip velocity reveals remarkable consistency. For structures with relatively large permeability values ( $\sqrt{K}/H > 0.05$ ), the slip velocity exhibits a linear relationship with the square root of permeability. In contrast, for less permeable structures ( $\sqrt{K}/H < 0.05$ ), the slip velocity tends to surpass the values predicted by this linear trend. This deviation becomes more pronounced as the permeability decreases. Predictions from the BDL model with the linear equation  $\gamma = 2\epsilon$  align well with the simulation results. Nevertheless, predictions from the BDL model turn a little smaller for structures with relatively low permeability values than the simulation results, which could be attributed to the interpolation error when calculating slip velocity. Since the slip velocity was calculated by interpolating the velocity of neighboring nodes, it may deviate more from the actual slip velocity in less permeable structures with smaller slip velocity values.

The interface layer thickness also demonstrates a linear relationship with the square root of permeability, consistent with the predictions of the BDL model. However, larger scatterings are observed in structures with higher permeabilities, which can be attributed to random variations in the microstructure introduced by stochastic factors in the growth algorithm. The interface layer thickness, being highly sensitive to microstructures in the vicinity of the interface, is more susceptible to contingencies in sparser fibrous structures. Consequently, accidental fiber clusters or cavities are more likely to lead to observable scatterings in the interface layer thickness for structures with high permeability values.

The two shear stresses are nondimensionalized by the shear stress at the wall in a Poiseuille flow with the same channel height and pressure gradient. The shear stress from the channel side exhibits the

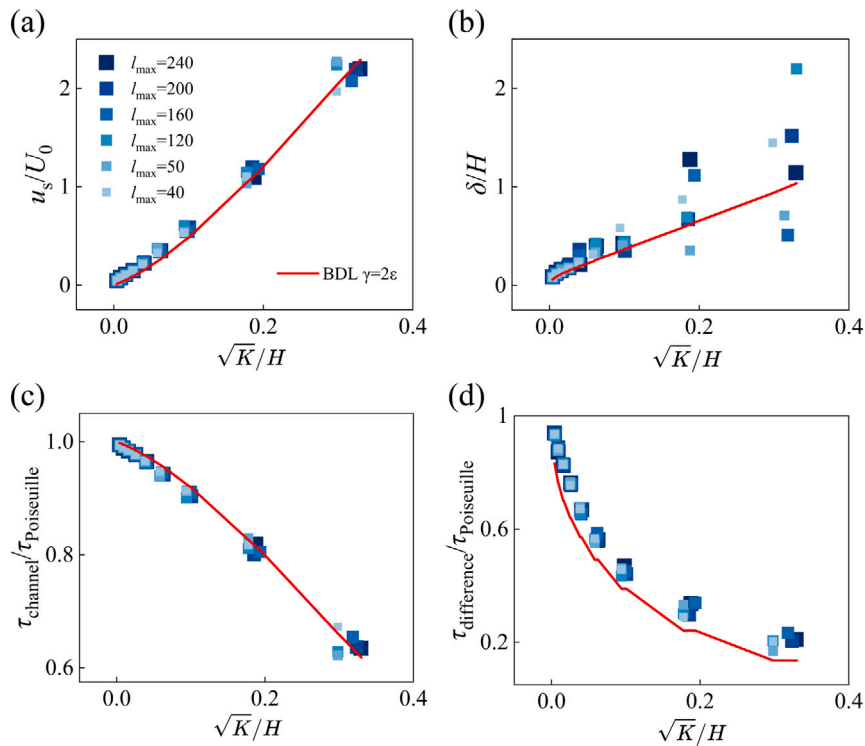


Fig. 5. Variations of (a) slip velocity, (b) interface layer thickness, (c) shear stress from the channel side at the free-fibrous interface, and (d) shear stress difference at the free-fibrous interface against the square root of permeability for naturally grown straight fibrous structures. Symbols of different sizes and shades represent different fiber lengths. The red solid lines represent the BDL model with  $\gamma = 2\epsilon$ .  $U_0$  and  $\tau_{Poiseuille}$  stand for the average velocity and shear stress at the wall in Poiseuille flow with the same channel height and pressure gradient, respectively.  $H$  stands for the channel height.

most pronounced linearity among all four parameters studied (Fig. 5c), and predictions by the BDL model also maintain the best agreement. As the permeability increases, the corresponding shear stress decreases. When the permeability tends to zero, the dimensionless shear stress approaches unity, signifying a scenario where the fiber network behaves like a solid wall effectively. As the permeability of the fibrous porous structures increases, the data points in the shear stress plot become slightly more dispersed. This increased scattering is attributed to the heightened sensitivity of interfacial properties to the inherent randomness in sparser fibrous structures.

The results concerning the shear stress difference, denoted as  $\tau_{difference}$ , have yielded remarkably consistent findings for all naturally grown straight fibrous structures. As depicted in Fig. 5(d), the dimensionless shear stress difference initially exhibits a rapid decline from 1, followed by deceleration, and eventually converges towards zero with increasing permeability. Even in high-permeability cases, data points representing different structures cluster closely together, highlighting the robustness of this parameter in capturing the underlying dynamics within complex fibrous porous structures. Moreover, the shear stress from the channel side consistently surpasses that from the porous side in these free-fibrous coupled systems (the difference remains above zero), revealing the force balance at the free-porous interface. Predictions of the BDL model also show good agreement with the simulation results, although they tend to underestimate it a little bit. Given the sensitivity of this parameter, the BDL model still provides satisfactory results.

Results of the structures comprising randomly piled cylinders of the same aspect ratio are illustrated in Fig. 6, in which green triangles represent individual structures and red solid lines represent the BDL model. The results of structures with the porosity value of 0.99 were also neglected due to the over-scattering in interface layer thickness.

Remarkably, the four parameters exhibit precisely the same trends with respect to permeability as the naturally grown fibers, and the BDL model also maintains good agreement with the simulation results.

However, larger scatterings are observed for highly permeable structures in the first three parameters in comparison to the naturally grown fibers, highlighting the influence of the fiber length distribution on fluid transport.

In summary, the BDL model with the linear equation  $\gamma = 2\epsilon$  accurately captures the interfacial flow dynamics in both types of isotropic fibrous porous structures, regardless of porosity, permeability, or fiber length.

#### 4.2. Anisotropic fibrous structures

In addition to the above isotropic fibrous porous structures, we generated two types of anisotropic fibrous structures, including the layered and aligned variants.

In the layered fibrous structures, we constrained the polar angle within the range  $[\pi/2 - \Delta\theta, \pi/2 + \Delta\theta]$  to create anisotropy. Smaller values of  $\Delta\theta$  correspond to more neatly layered structures, thus higher degrees of anisotropy (Fig. 7a) and vice versa (Fig. 7b). Six different values for  $\Delta\theta$  have been selected:  $\pi/4, \pi/5, \pi/6, \pi/8, \pi/16, \pi/32$ . The azimuthal angle  $\phi$  was evenly distributed within the range  $[0, 2\pi]$ . For each value of  $\Delta\theta$ , we generated nine individual structures with varying porosity values, ranging from 0.2 to 0.95. The fiber length distributions also exhibit Gaussian patterns with a maximum of 120 lattice units.

The permeability of the layered fibrous porous structures also follows a three-stage curve against porosity, akin to the isotropic fibrous structures. The anisotropy has a minor influence on permeability by increasing the longitudinal permeability with larger  $\Delta\theta$  values. This increment turns larger for denser fibrous structures (Fig. 6d).

The four parameters characterizing the interfacial transport have also been studied, and comparisons between the BDL model and pore-scale simulations are shown in Fig. 8. The yellow diamonds with different shades and sizes represent the layered fibrous structures of various anisotropy, and the solid red lines represent the BDL model.

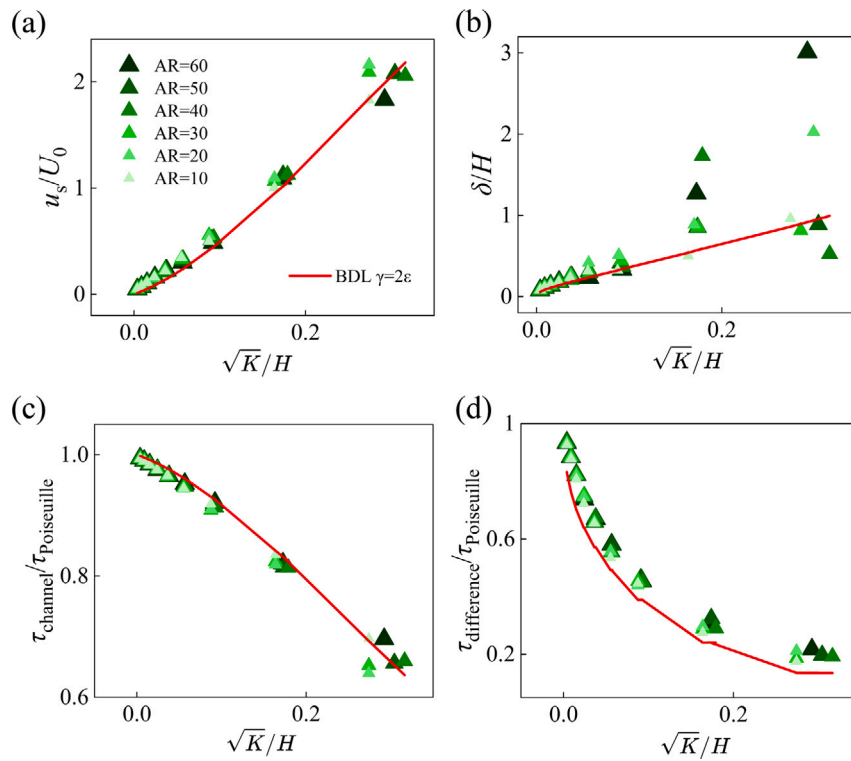


Fig. 6. Variations of (a) slip velocity, (b) interface layer thickness, (c) shear stress from the channel side at the free-fibrous interface, and (d) shear stress difference at the free-fibrous interface with respect to the square root of permeability for randomly piled cylinders. The red solid lines represent the BDL model with  $\gamma = 2\epsilon$ .  $U_0$  and  $\tau_{\text{Poiseuille}}$  stand for the average velocity and shear stress at the wall in Poiseuille flow with the same channel height and pressure gradient, respectively.  $H$  stands for the channel height.

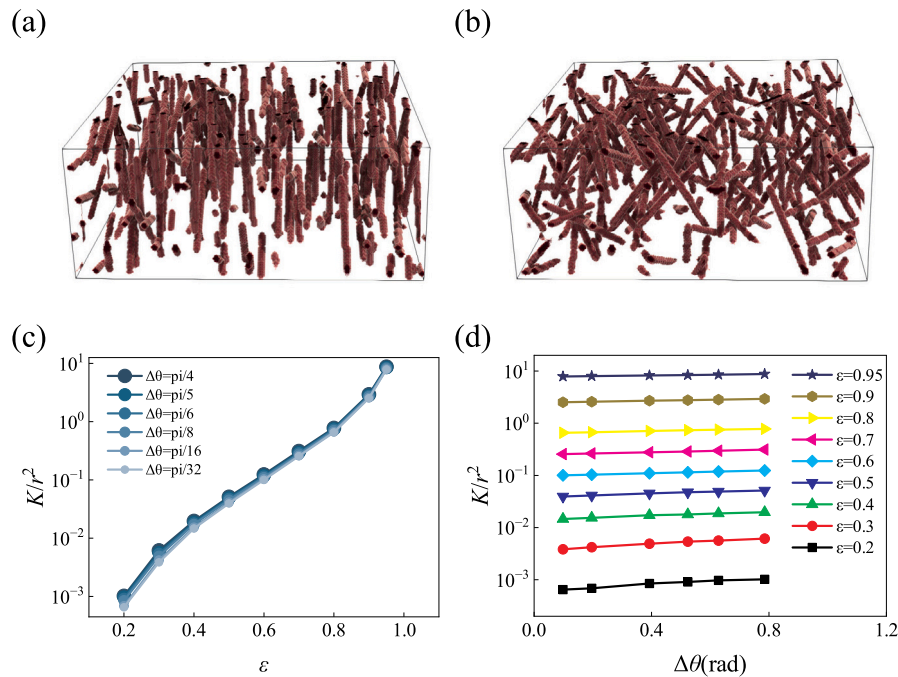


Fig. 7. Schematic diagram of layered fibrous structures with (a)  $\Delta\theta = \pi/32$  and (b)  $\Delta\theta = \pi/4$ . Variations of permeability with respect to porosity (c) and  $\Delta\theta$  (d).  $r$  stands for the radius of the fibers.

Though the morphology of the layered fibrous structures differs significantly from the isotropic ones, the four parameters show the same linear and nonlinear trends against permeability. Scatterings of results in large-permeability structures are much less than those observed in isotropic structures, owing to the strong structural anisotropy.

Nevertheless, the BDL model again offers satisfactory predictions in all four parameters. The shear stress difference turns a little larger than predicted due to the decreased shear force in layered fibrous structures compared to isotropic ones, but the trend stays the same.

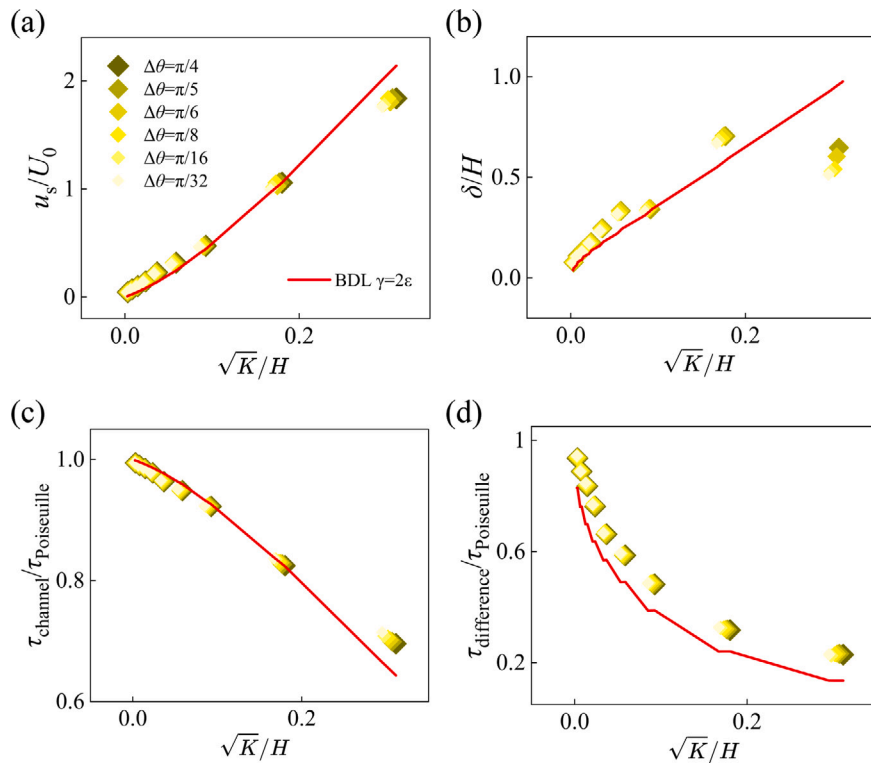


Fig. 8. Variations of (a) slip velocity, (b) interface layer thickness, (c) shear stress from the channel side at the free-fibrous interface, and (d) shear stress difference at the free-fibrous interface with respect to the square root of permeability for layered fibrous porous structures. Symbols of different sizes and shades represent different anisotropy. The red solid lines represent the BDL model with  $\gamma = 2\epsilon$ .

Regarding the aligned fibrous structures, fiber orientations were deliberately set to remain parallel (or nearly parallel) to the flow direction (z-axis), achieved by assigning a maximum polar angle value denoted as  $\theta_{max}$ . By changing this value, we created aligned fibrous structures with varying degrees of anisotropy. When reducing  $\theta_{max}$ , the fibers became more aligned, and vice versa. Illustrated in Fig. 9(a,b) are two examples ranging from fully parallel structure ( $\theta_{max} = 0$ ) to weakly aligned structure ( $\theta_{max} = \pi/3$ ). We selected five values for  $\theta_{max}$ :  $0, \pi/12, \pi/6, \pi/4, \pi/3$ . For each value, nine distinct fibrous porous structures were generated, with porosity values varying from 0.2 to 0.95. By limiting the maximum fiber length to 120 (lattice units) and choosing moderate fiber densities, fiber length distributions of these structures also show Gaussian distribution patterns. To ensure isotropy in the x-y plane, the azimuthal angle was evenly distributed within the range  $[0, 2\pi]$ .

The permeability of aligned fibrous structures also shows a three-stage inverse ‘‘S’’ pattern against porosity but exhibits more significant variations under low-porosity conditions (Fig. 9c). The degree of alignment of fibers directly impacts the permeability of the network. For instance, the permeability of the fully parallel fibrous structure with a porosity of 0.2 is nearly ten times larger than that of the least aligned structure with the same porosity value. However, for high-porosity structures, the difference in permeability between the aligned fibrous structures becomes negligible. By plotting against the maximum polar angle (demonstrated in Fig. 9d), the correlation between permeability and the degree of fiber alignment is more explicitly highlighted, revealing the drastic changes in fiber morphology.

Even with such diverse microstructures, the results of the four parameters almost remain unchanged. As illustrated in Fig. 10, stars with distinct shades and sizes stand for aligned fibrous structures of different anisotropy, and the red solid lines stand for the BDL model. The first three parameters exhibit strong linearity regarding the square root of permeability, while the last one shows a hyperbolic curvature. Predictions by the BDL model still maintain good agreement

with simulation results. However, a decrease is observed in interface layer thickness for highly permeable structures, suggesting the aligned structure could decrease  $\delta$  in sparse fiber matrixes.

In general, despite the strong anisotropy and diverse microstructures displayed in both types of anisotropic fibrous structures, the four parameters show the same trend, and the BDL model reveals great consistency in comparison with simulation results.

### 4.3. Tortuous fibrous structures

Moreover, another type of fibrous porous structure featuring random tortuosity was generated, simulating the presence of curved fibrous structures in natural systems. These tortuous fibrous structures were generated based on the randomly grown straight fibers but were decorated by adding random deflections in the orientation angle during each growing time step. The degree of fiber tortuosity could be manipulated by controlling the maximum deflection angle denoted as  $\zeta$ . Fig. 10(a) and (b) showcase two example structures with the same porosity and maximum fiber length but different fiber tortuosity. Larger maximum deflection angles correspond to more curved fibers and vice versa.

We set the maximum length of the fibers to  $l_{max} = 40, 80, 120, 160$ , along with four values for the maximum deflection angle:  $\zeta = \pi/4, \pi/8, \pi/16, \pi/32$ . For each combination, nine distinct structures with porosity ranging from 0.2 to 0.95 were generated. All structures exhibit Gaussian fiber length distribution patterns by manipulating fiber density.

The permeability of the tortuous fibrous structures also exhibits the three-stage inverse ‘‘S’’ pattern in the  $K - \epsilon$  plot. In Fig. 11(c), each color represents a different maximum deflection angle, while varying shades and symbol sizes correspond to different fiber lengths. As anticipated, the fiber length has no discernible impact on permeability in these structures.

However, an unexpected increment in permeability with fiber tortuosity was observed. The permeability of structures with the largest

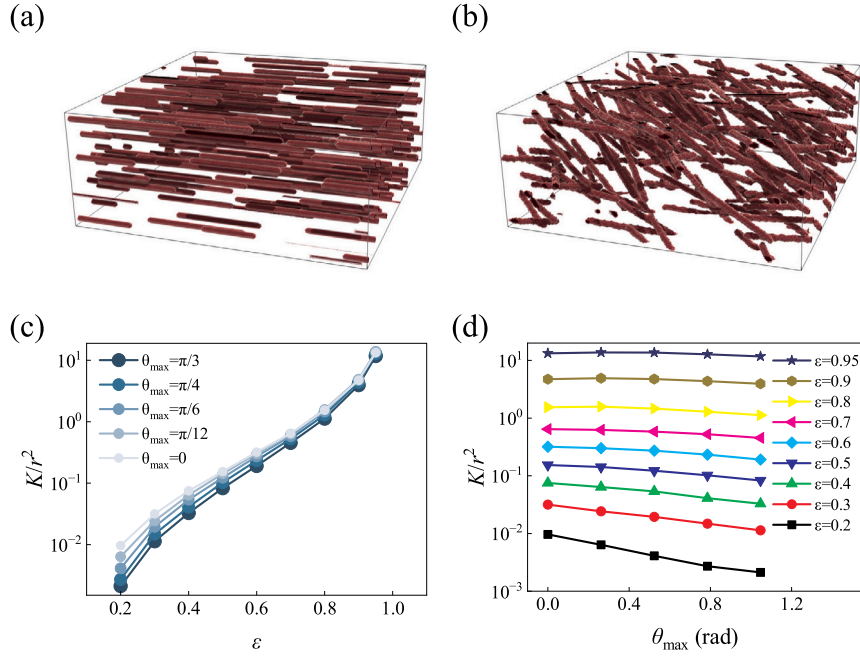


Fig. 9. Schematic diagram of (a) aligned fibrous structures with  $\theta_{\max} = 0$  and (b)  $\theta_{\max} = \pi/3$ . Variations of permeability with respect to porosity (c) and  $\theta_{\max}$  (d).  $r$  stands for the radius of the fibers.

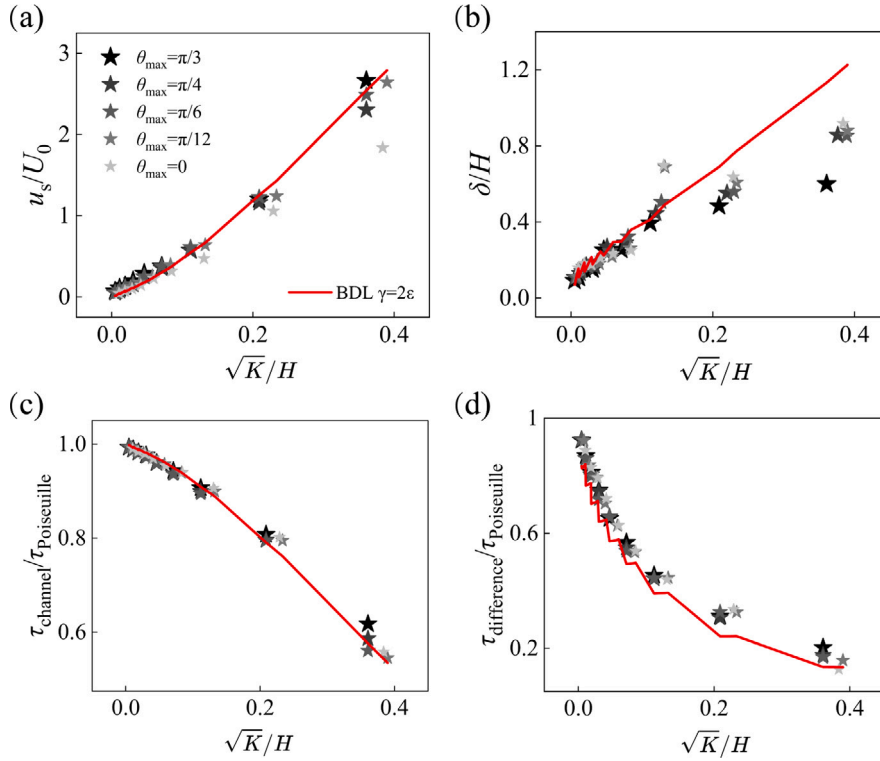


Fig. 10. Variations of (a) slip velocity, (b) interface layer thickness, (c) shear stress from the channel side at the free-fibrous interface, and (d) shear stress difference at the free-fibrous interface with respect to the square root of permeability for aligned fibrous porous structures. Symbols of different sizes and shades represent different anisotropy. The red solid lines represent the BDL model with  $\gamma = 2\epsilon$ .

tortuosity is approximately 10% higher than those with minimal tortuosity, which is a noticeable difference.

To provide a deeper insight into this phenomenon, we explored the alteration of anisotropy within the tortuous fibrous structures quantitatively. For this purpose, we adopted the following definition of the second-order fiber orientation tensor, which has been described

elsewhere [58]:

$$\Omega = \frac{1}{I_{\text{tot}}} \sum I_i \begin{bmatrix} \sin^2 \theta_i \cos^2 \phi_i & \sin^2 \theta_i \sin \phi_i \cos \phi_i & \cos \theta_i \sin \theta_i \cos \phi_i \\ \sin^2 \theta_i \sin \phi_i \cos \phi_i & \sin^2 \theta_i \sin^2 \phi_i & \cos \theta_i \sin \theta_i \cos \phi_i \\ \cos \theta_i \sin \theta_i \cos \phi_i & \cos \theta_i \sin \theta_i \cos \phi_i & \cos^2 \theta_i \end{bmatrix}, \quad (13)$$

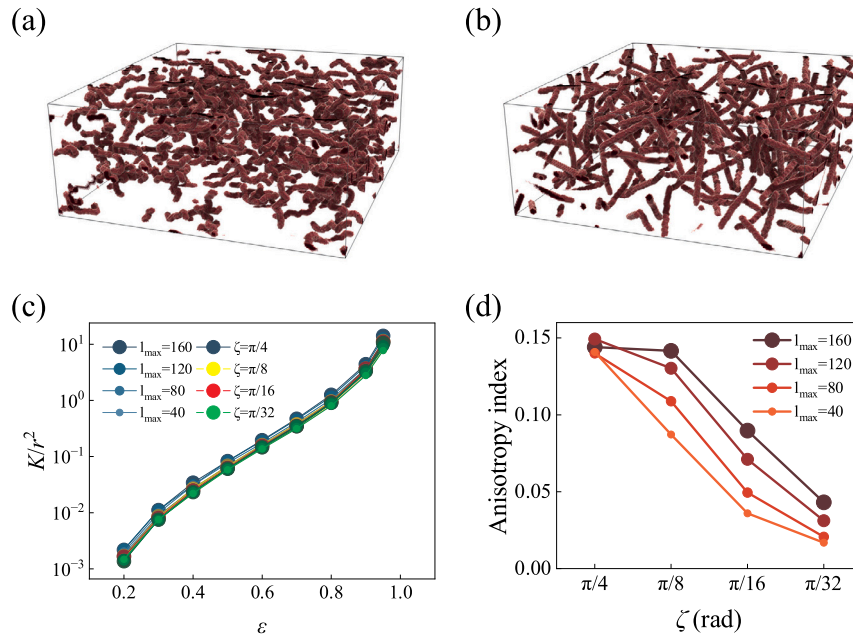


Fig. 11. Schematic diagram of (a) tortuous fibrous structures with  $\zeta = \pi/4, l_{\max} = 120, \epsilon = 0.95$  and (b) tortuous fibrous structures with  $\zeta = \pi/32, l_{\max} = 120, \epsilon = 0.95$ . (c) Variations of permeability with respect to porosity.  $r$  stands for the radius of the fibers. (d) Various degrees of anisotropy induced by different maximum deflection angle  $\xi$ .

Table 1

The anisotropy property and the range of the polar and azimuthal angles for the five types of fibrous structures generated.

Name	Anisotropy	$\theta$	$\phi$
Aligned structure	Anisotropic	$[0, \theta_{\max}]$	$[0, 2\pi]$
Layered structure	Anisotropic	$[\pi/2 - \Delta\theta, \pi/2 + \Delta\theta]$	$[0, 2\pi]$
Naturally grown straight fibers	Isotropic	$[0, \pi]$	$[0, 2\pi]$
Randomly pile cylinders	Isotropic	$[0, \pi]$	$[0, 2\pi]$
Tortuous fibers	Anisotropic	$[0, \pi]$	$[0, 2\pi]$

where  $l_i$  stands for the length of the  $i^{\text{th}}$  fiber,  $l_{\text{tot}}$  stands for the total fiber length. The three diagonal elements should equal  $1/3$  if the fibrous structure is perfectly isotropic in 3D. To further quantify the anisotropy of fibrous structures, we proposed an anisotropy index, defined as the standard deviation of the three diagonal elements. A larger anisotropy index indicates a more anisotropic fiber network and vice versa. The anisotropy of curved fibrous structures with a porosity of 0.5 has been evaluated by this index. As shown in Fig. 11(d), the structure anisotropy increases with the increase of fiber tortuosity. Moreover, the fiber length also influences anisotropy to a certain extent, as longer fibers have greater chances of having curvatures and, thus, are more likely to be anisotropic.

The findings in Fig. 10(d) demonstrate that random curvatures during the growth process significantly contribute to the anisotropy in initially isotropic fibrous structures. As many fibrous structures encountered in real-life applications exhibit tortuous characteristics, avoiding oversimplifications and accounting for the inherent anisotropy is crucial to obtaining reliable and accurate results.

Results of the four parameters for tortuous fibrous structures are presented in Fig. 12, in which different shades stand for different fiber lengths and distinct shapes and colors stand for various tortuosity.

The four parameters in tortuous fibrous structures still show the same patterns as all four types of structures above, and predictions of the BDL model maintain good agreement with the simulation results.

The anisotropy property and generation parameters of the above five types of fibrous structures are listed in Table 1. The outcomes related to the four key parameters reveal a striking consistency across

all five types of fibrous porous structures, each characterized by diverse microstructures. Both linear and nonlinear patterns observed in these fibrous structures closely resemble those reported in common granular porous structures [31]. One may notice that there are stepwise behaviors in the results of the shear stress difference, which are mainly due to the randomness of the fibrous structures grown by our stochastic method. Two structures having the same porosity value may have different permeability values, while predictions by the BDL model tend to be similar owing to the limitation of the number of input model parameters. This phenomenon is more evident in fibrous structures grown more arbitrarily. However, the model still provides satisfying predictions in that the shear stress difference is very sensitive to the boundary morphology of the porous media. In general, the above results suggest that these parameters can unveil underlying mechanisms in free-porous coupled flow systems, possibly regardless of the structure types. Notably, the BDL model with the linear expression for model parameter  $\gamma = 2\epsilon$  offers accurate and stable predictions of all four parameters in all types of fibrous structures, revealing its robustness in capturing the interfacial transport dynamics even in complex fibrous porous structures with diverse anisotropy.

#### 4.4. Influence of other factors

In addition to the dominant factor of structural morphology, we conducted further investigations to explore the impact of other potential factors. Specifically, the influence of pressure gradient, flow shear rate, and fluid viscosity has been examined to find out whether the BDL model is still valid when altering these flow conditions. To investigate these effects, pore-scale flow simulations were carried out in five selected fibrous structures, each belonging to a distinct type. The detailed properties of these structures are presented in Table 2.

To investigate the impact of pressure gradient, we conducted simulations by varying the original pressure gradient, denoted as  $\nabla P_0$ , within the range of  $[0.01\nabla P_0, 10\nabla P_0]$ . Results of the four parameters are presented in Fig. 13.

Overall, all four parameters remained largely unaffected by the pressure gradient across the selected fibrous structures. However, a minor decrease is observed in cases with large pressure gradients for

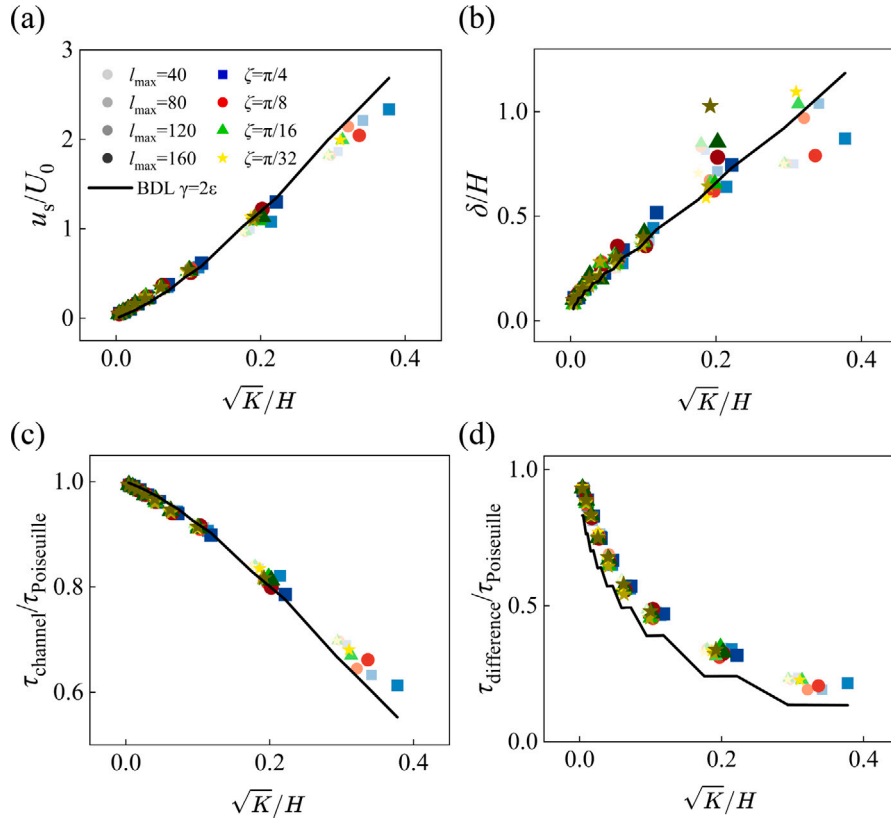


Fig. 12. Variations of (a) slip velocity, (b) interface layer thickness, (c) shear stress from the channel side at the free-fibrous interface, and (d) shear stress difference at the free-fibrous interface with respect to the square root of permeability for tortuous fibrous structures. Symbols of different shades represent different fiber lengths, and different colors and shapes represent different tortuosity. The solid lines represent the BDL model with  $\gamma = 2\epsilon$ .

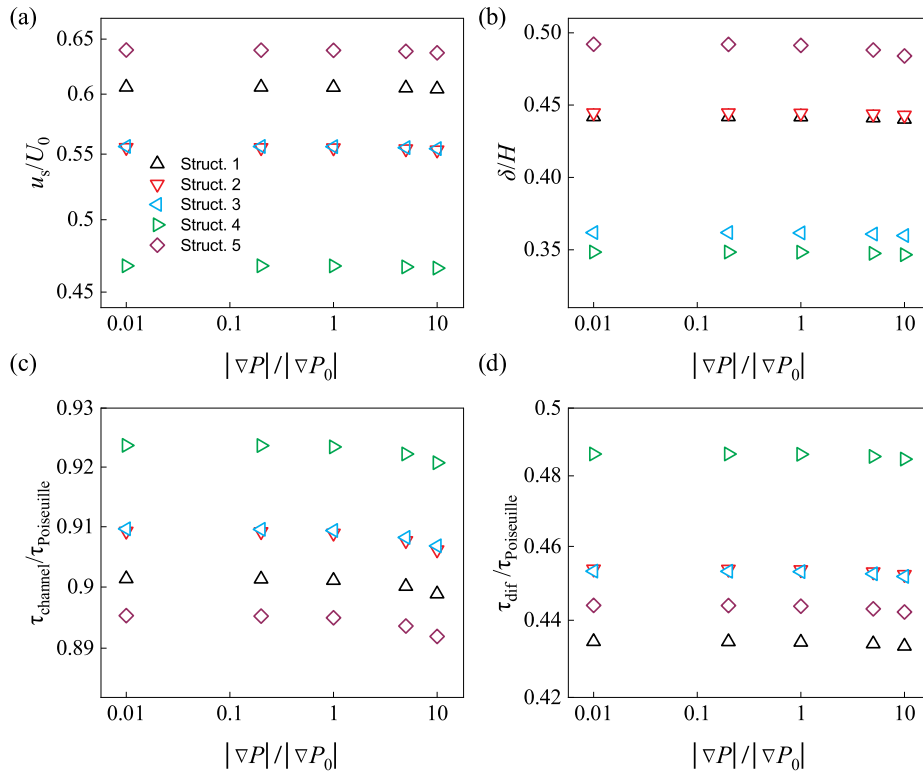


Fig. 13. Influence of the pressure gradient on the four key parameters: (a) slip velocity, (b) interface layer thickness, (c) shear stress on the channel side, and (d) shear stress difference at the free-fibrous interface.  $\nabla P_0$  stands for the original pressure gradient value.

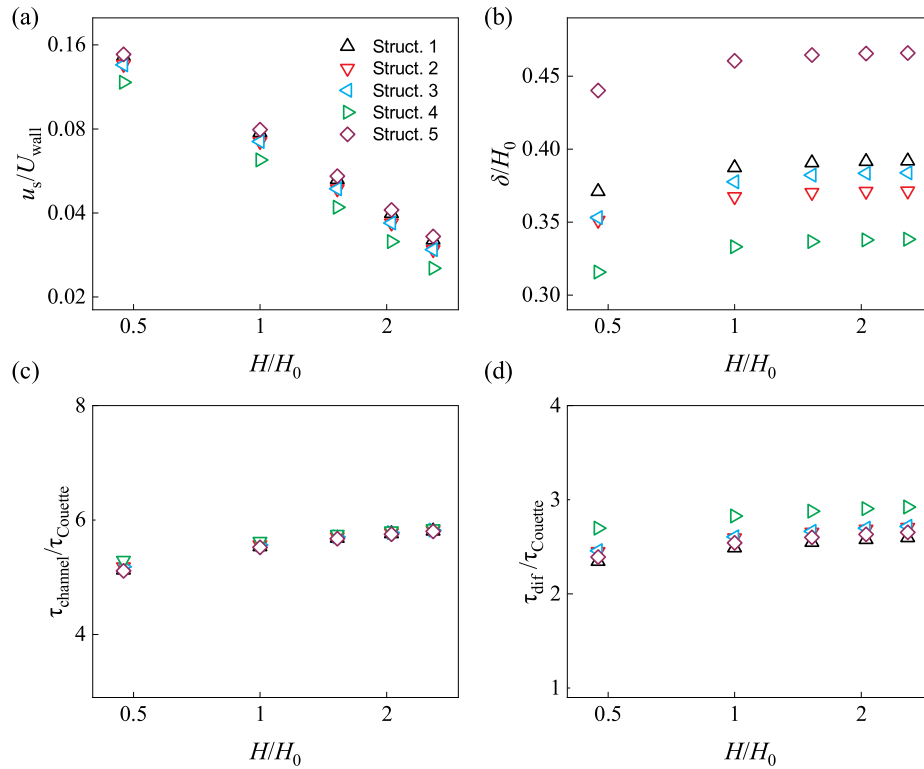


Fig. 14. Influence of the fluid shear rate on the four key parameters: (a) slip velocity, (b) interface layer thickness, (c) shear stress on the channel side, and (d) shear stress difference at the free-fibrous interface.  $H_0$  stands for the original channel height.

Table 2

The value of porosity, cluster size, and permeability of the porous structures in the five selected coupled systems.

Name	Porosity	Type	Permeability (D)	Mean fiber length
Struct.1	0.8	Naturally grown	128.9	60
Struct.2	0.8	Piled cylinders	108.8	60
Struct.3	0.8	tortuous	138.7	60
Struct.4	0.8	Layered	105.6	60
Struct.5	0.8	aligned	210.7	60

the interface layer thickness and shear stress from the channel side. This phenomenon can be attributed to the increase in the Reynolds number ( $Re$ ) under such conditions. As the permeability of the selected structure is considerably large, the  $Re$  approaches the Stokes limit under large pressure gradients. Nonetheless, since this reduction is barely noticeable ( $< 1\%$ ), and the present study was conducted under the Stokes assumption, it can still be concluded that the pressure gradient does not significantly influence the interfacial flow behavior, and the BDL model should still be valid under different pressure gradients as long as the Reynolds number is not too large (model assumption).

The fluid shear rate has been considered as a potential factor because the  $u_s/\gamma\sqrt{K}$  has been reported as a key dimensionless parameter in some previous studies [59,60]. To clarify this, we conducted simulations of shear-driven flows with fixed wall velocity but varying channel heights while keeping other simulation parameters unchanged. The shear rate at the interface was estimated by the ratio of wall velocity over the channel height. The results are presented in Fig. 14.

In the logarithmic plot shown in Fig. 14(a), the slip velocity exhibits an inverse linear relationship with the channel height, indicating it is

proportional to the fluid shear rate. Conversely, the other three parameters remain relatively unchanged except in the cases of the lowest channel height. This phenomenon can be attributed to the violation of the length constraint on such free-porous systems — the channel height should be significantly larger than the pore sizes [25,61]. Since the porosity values of the chosen structures are large, the equivalent “pore diameters” are also substantial, approaching the decreasing channel height. This deduction is verified by the fact that the results of Struct.4, with the smallest “pore diameter”, show the smallest derivation when  $H = 0.5H_0$  while the results of Struct.5, with the largest “pore diameter”, show the largest. This phenomenon is more obvious with the shear stress from the channel side, as illustrated by Fig. 14(c). The results indicate that the fluid shear rate primarily influences the slip velocity, while the other parameters remain relatively unaffected. In the derivation of the stress-jump condition of the BDL model, the shear stress has taken the form of a linear function of slip velocity, which coincides with the above findings. This suggests that the BDL model should be valid with varying fluid shear rates.

Finally, the impact of the fluid viscosity was studied by varying the dimensionless viscosity from 0.01 to 10 (the origin value  $\mu_0 = 1/6$  corresponding to the viscosity of water) in pressure-driven flows. The results are presented in Fig. 15. Generally, all four parameters remain unaffected by fluid viscosity, with only a few isolated points deviating from this trend, likely owing to the specific characteristics of certain structures. This suggests the BDL model would be valid with a large range of fluid viscosity values.

In summary, our investigations demonstrate that only the fluid shear rate exhibits a proportional relationship with the slip velocity, while the other parameters have little impacts on the interfacial flow behavior in the coupled system. The Brinkman double-layer (BDL)

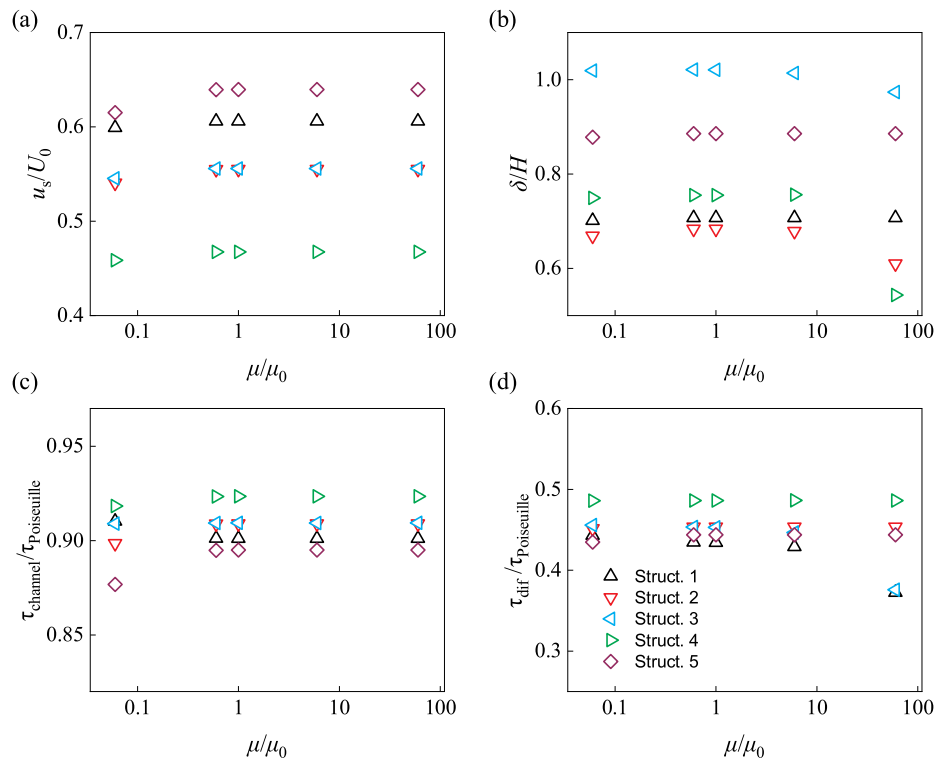


Fig. 15. Influence of the fluid viscosity on the four key parameters: (a) slip velocity, (b) interface layer thickness, (c) shear stress on the channel side, and (d) shear stress difference at the free-fibrous interface.  $\mu_0$  stands for the original fluid viscosity.

model, validated across various types of fibrous structures, can accurately capture the interfacial transport behavior irrespective of the flow conditions, as long as the flow system meets the constraints on length scale and Reynolds number. Despite the fact that the linear expression for the model parameter  $\gamma$  was initially derived for granular porous media, the results above highlight its effectiveness in complex fibrous porous structures. These findings further broaden the applicability of the Brinkman double-layer (BDL) model, suggesting its robustness in modeling interfacial flow dynamics in fibrous porous structures with intricate microstructures and varying degrees of anisotropy. However, the applicability of the BDL model in much more complex scenarios like complex interface patterns, transient flow, etc., remains to be further studied.

### 5. Conclusions

This study has conducted a comprehensive numerical investigation on the interfacial transport behavior and an assessment of the Brinkman double-layer (BDL) model in free-fibrous coupled systems comprising 3D fibrous structures with complex geometries.

Various fibrous porous structures have been regenerated by the Random Generation Growth (RGG) algorithm, encompassing both isotropic and anisotropic features with diverse porosity values. The substantial variation in permeability underscores the pronounced differences in fiber morphology among these structures. A free-fibrous coupled flow system is created with each fibrous structure by parallelly bounding a straight, clean channel on top. High-performance pore-scale simulations have been implemented within the pores and the channel. Compared with the other previous models for the interfacial transport, the BDL model with a linear expression for the model parameter  $\gamma = 2\epsilon$  exhibited the best consistency across all types of fibrous structures, accurately agreeing with the results of pore-scale simulations, regardless of structural anisotropy. Moreover, the influence from other potential influential factors has also been examined, further affirming

the applicability of the BDL model with diverse pressure gradients, flow shear rates, and fluid viscosity values.

In conclusion, the BDL model can successfully capture the essential dynamics and demonstrate general validity and robustness in free-fibrous coupled flow systems. The linear expression for the model parameter  $\gamma$  has proven to be applicable in fibrous structures with diverse degrees of anisotropy despite being originally derived from granular porous structures.

### CRedit authorship contribution statement

**Jinliang Kang:** Writing – original draft, Validation, Investigation.  
**Moran Wang:** Writing – review & editing, Supervision, Conceptualization.

### Declaration of competing interest

The authors declare that they have no known competing financial interests or personal relationships that could have appeared to influence the work reported in this paper.

### Data availability

No data was used for the research described in the article.

### Acknowledgments

This work is financially supported by the NSF of China (No. 12272 207), the National Key R and D Program of China (No. 2019YFA0708 704), and the Tsinghua University Initiative Scientific Research Program, China.

## References

- [1] C. Broedersz, F. MacKintosh, Modeling semiflexible polymer networks, *Rev. Mod. Phys.* 57 (8) (2014) 1492–1704.
- [2] X. Wang, B. Ding, G. Sun, M. Wang, J. Yu, Electro-spinning/netting: A strategy for the fabrication of three-dimensional polymer nano-fiber/nets, *Prog. Mater. Sci.* 58 (2013) 1173–1243.
- [3] I.D. Patiño, H. Power, C. Nieto-Londoño, W.F. Flórez, Stokes–Brinkman formulation for prediction of void formation in dual-scale fibrous reinforcements: a BEM/DR-BEM simulation, *Comput. Mech.* 59 (4) (2017) 555–577, <http://dx.doi.org/10.1007/s00466-016-1360-5>.
- [4] F. Habel, C. Mendoza, A.C. Bagtzoglou, Solute transport in open channel flows and porous streambeds, *Adv. Water Resour.* 25 (4) (2002) 455–469, [http://dx.doi.org/10.1016/s0309-1708\(01\)00052-5](http://dx.doi.org/10.1016/s0309-1708(01)00052-5).
- [5] P. Verboven, D. Flick, B. Nicolai, G. Alvarez, Modelling transport phenomena in refrigerated food bulks, packages and stacks: basics and advances, *Int. J. Refrig.* 29 (6) (2006) 985–997, <http://dx.doi.org/10.1016/j.ijrefrig.2005.12.010>.
- [6] M.A.V. Doormaal, J.G. Pharoah, Determination of permeability in fibrous porous media using the lattice Boltzmann method with application to PEM fuel cells, *Internat. J. Numer. Methods Fluids* 59 (1) (2009) 75–89, <http://dx.doi.org/10.1002/flid.1811>.
- [7] X. He, Y. Guo, M. Li, N. Pan, M. Wang, Effective gas diffusion coefficient in fibrous materials by mesoscopic modeling, *Int. J. Heat Mass Transfer* 107 (2017) 736–746, <http://dx.doi.org/10.1016/j.ijheatmasstransfer.2016.11.097>.
- [8] S. Mahjoob, K. Vafai, A synthesis of fluid and thermal transport models for metal foam heat exchangers, *Int. J. Heat Mass Transfer* 51 (15–16) (2008) 3701–3711, <http://dx.doi.org/10.1016/j.ijheatmasstransfer.2007.12.012>.
- [9] J. Hyvältuoma, P. Raiskinmäki, A. Jäsberg, A. Koponen, M. Kataja, J. Timonen, Simulation of liquid penetration in paper, *Phys. Rev. E* 73 (3) (2006) 036705, <http://dx.doi.org/10.1103/physreve.73.036705>.
- [10] V.P. Chauhan, T. Stylianopoulos, Y. Boucher, R.K. Jain, Delivery of molecular and nanoscale medicine to tumors: Transport barriers and strategies, *Chem. Biomol. Eng.* 2 (1) (2011) 281–298, <http://dx.doi.org/10.1146/annurev-chembioeng-061010-114300>.
- [11] A. Jarauta, V. Zingan, P. Minev, M. Secanell, A compressible fluid flow model coupling channel and porous media flows and its application to fuel cell materials, *Transp. Porous Media* 134 (2) (2020) 351–386, <http://dx.doi.org/10.1007/s11242-020-01449-2>.
- [12] F.J. Valdés-Parada, D. Lasseux, A novel one-domain approach for modeling flow in a fluid-porous system including inertia and slip effects, *Phys. Fluids* 33 (2) (2021) 022106, <http://dx.doi.org/10.1063/5.0036812>.
- [13] E. Eggenweiler, I. Rybak, Effective coupling conditions for arbitrary flows in Stokes–Darcy systems, *Multiscale Model. Simul.* 19 (2) (2021) 731–757, <http://dx.doi.org/10.1137/20M1346638>.
- [14] S.B. Naqvi, A. Bottaro, Interfacial conditions between a free-fluid region and a porous medium, *Int. J. Multiph. Flow* 141 (2021) 103585, <http://dx.doi.org/10.1016/j.ijmultiphaseflow.2021.103585>, URL: <https://www.sciencedirect.com/science/article/pii/S0301932221000331>.
- [15] P. Angot, B. Goyeau, J.A. Ochoa-Tapia, Asymptotic modeling of transport phenomena at the interface between a fluid and a porous layer: Jump conditions, *Phys. Rev. E* 95 (2017) 063302, <http://dx.doi.org/10.1103/PhysRevE.95.063302>, URL: <https://link.aps.org/doi/10.1103/PhysRevE.95.063302>.
- [16] A. Bottaro, Flow over natural or engineered surfaces: an adjoint homogenization perspective, *J. Fluid Mech.* 877 (2019) P1, <http://dx.doi.org/10.1017/jfm.2019.607>.
- [17] Z. Xu, J. Zhang, Y.-N. Young, P. Yue, J.J. Feng, Comparison of four boundary conditions for the fluid-hydrogel interface, *Phys. Rev. Fluids* 7 (2022) 093301, <http://dx.doi.org/10.1103/PhysRevFluids.7.093301>, URL: <https://link.aps.org/doi/10.1103/PhysRevFluids.7.093301>.
- [18] G.S. Beavers, D.D. Joseph, Boundary conditions at a naturally permeable wall, *J. Fluid Mech.* 30 (1) (1967) 197–207, <http://dx.doi.org/10.1017/S0022112067001375>.
- [19] P.G. Saffman, On the boundary condition at the surface of a porous medium, *Stud. Appl. Math.* 50 (2) (1971) 93–101, <http://dx.doi.org/10.1002/sapml197150293>.
- [20] B. Goyeau, D. Lhuillier, D. Gobin, M. Velarde, Momentum transport at a fluid-porous interface, *Int. J. Heat Mass Transfer* 46 (21) (2003) 4071–4081, [http://dx.doi.org/10.1016/S0017-9310\(03\)00241-2](http://dx.doi.org/10.1016/S0017-9310(03)00241-2), URL: <https://www.sciencedirect.com/science/article/pii/S0017931003002412>.
- [21] W.P. Breugem, B.J. Boersma, R.E. Uittenbogaard, The laminar boundary layer over a permeable wall, *Transp. Porous Media* 59 (3) (2005) 267–300, <http://dx.doi.org/10.1007/s11242-004-2557-1>.
- [22] M.L. Bars, M.G. Worster, Interfacial conditions between a pure fluid and a porous medium: implications for binary alloy solidification, *J. Fluid Mech.* 550 (1) (2006) 149–173, <http://dx.doi.org/10.1017/s0022112005007998>.
- [23] H.C. Brinkman, A calculation of the viscous force exerted by a flowing fluid on a dense swarm of particles, *Flow Turbul. Combust.* 1 (1) (1949) 27, <http://dx.doi.org/10.1007/bf02120313>.
- [24] G. Neale, W. Nader, Practical significance of Brinkman’s extension of darcy’s law: Coupled parallel flows within a channel and a bounding porous medium, *Can. J. Chem. Eng.* 52 (4) (1974) 475–478, <http://dx.doi.org/10.1002/cjce.5450520407>.
- [25] J. Ochoa-Tapia, S. Whitaker, Momentum transfer at the boundary between a porous medium and a homogeneous fluid—I. Theoretical development, *Int. J. Heat Mass Transfer* 38 (14) (1995) 2635–2646, [http://dx.doi.org/10.1016/0017-9310\(94\)00346-w](http://dx.doi.org/10.1016/0017-9310(94)00346-w).
- [26] P. Angot, On the well-posed coupling between free fluid and porous viscous flows, *Appl. Math. Lett.* 24 (6) (2011) 803–810, <http://dx.doi.org/10.1016/j.aml.2010.07.008>, URL: <https://www.sciencedirect.com/science/article/pii/S0893965910002521>.
- [27] H.X. Bai, P. Yu, S.H. Winoto, H.T. Low, Boundary conditions at the interface between fluid layer and fibrous medium, *Internat. J. Numer. Methods Fluids* 60 (7) (2009) 809–825, <http://dx.doi.org/10.1002/flid.1921>, URL: <https://onlinelibrary.wiley.com/doi/abs/10.1002/flid.1921>.
- [28] J. Alberto, Momentum jump condition at the boundary between a porous medium and a homogeneous fluid: inertial effects, *J. Porous Media* 1 (3) (1998) 201–217.
- [29] R.E. Larson, J.J.L. Higdon, Microscopic flow near the surface of two-dimensional porous media. Part 1. Axial flow, *J. Fluid Mech.* 166 (1986) 449–472, <http://dx.doi.org/10.1017/S0022112086000228>.
- [30] J.-L. Auriault, On the domain of validity of Brinkman’s equation, *Transp. Porous Media* 79 (2) (2009) 215–223, <http://dx.doi.org/10.1007/s11242-008-9308-7>.
- [31] J. Kang, M. Wang, Brinkman double-layer model for flow at a free-porous interface, *Int. J. Mech. Sci.* (2023) 108770, <http://dx.doi.org/10.1016/j.ijmecsci.2023.108770>, URL: <https://www.sciencedirect.com/science/article/pii/S0020740323006720>.
- [32] M. Wang, Q. Kang, N. Pan, Thermal conductivity enhancement of carbon fiber composites, *Appl. Therm. Eng.* 29 (2) (2009) 418–421, <http://dx.doi.org/10.1016/j.applthermaleng.2008.03.004>, URL: <https://www.sciencedirect.com/science/article/pii/S1359431108001312>.
- [33] H. Tan, X.-M. Chen, K.M. Pillai, T.D. Papathanasiou, Evaluation of boundary conditions at the clear-fluid and porous-medium interface using the boundary element method, *Evaluation* 8 (2008) 10.
- [34] V. Yerramalle, B. Premachandran, P. Talukdar, Numerical investigation of the performance of interface conditions for fluid flow through a partially filled porous channel, *Therm. Sci. Eng. Prog.* 20 (2020) 100628, <http://dx.doi.org/10.1016/j.tsep.2020.100628>, URL: <https://www.sciencedirect.com/science/article/pii/S2451904920301487>.
- [35] M. Mierzwiczak, A. Fraska, J.K. Grabski, Determination of the slip constant in the beavers-joseph experiment for laminar fluid flow through porous media using a meshless method, *Math. Probl. Eng.* 2019 (21) (2019) 1494215, <http://dx.doi.org/10.1155/2019/1494215>.
- [36] A. Terzis, I. Zarikos, K. Weishaupt, G. Yang, X. Chu, R. Helmig, B. Weigand, Microscopic velocity field measurements inside a regular porous medium adjacent to a low Reynolds number channel flow, *Phys. Fluids* 31 (4) (2019) 042001, <http://dx.doi.org/10.1063/1.5092169>.
- [37] C. Li, J. Huang, T. Qin, C. Chen, L. Gao, J. Xu, A novel approach to simulate the resin infusion process by two phases coupling free and porous flows intra and inter fiber tows of liquid composite molding, *J. Compos. Mater.* 56 (21) (2022) 3359–3367, <http://dx.doi.org/10.1177/00219983221111495>.
- [38] C. Delisée, J. Lux, J. Malvestro, 3D morphology and permeability of highly porous cellulose fibrous material, *Transp. Porous Media* 83 (3) (2010) 623–636, <http://dx.doi.org/10.1007/s11242-009-9464-4>.
- [39] P. Soltani, M.S. Johari, M. Zarrebini, Effect of 3D fiber orientation on permeability of realistic fibrous porous networks, *Powder Technol.* 254 (2014) 44–56, <http://dx.doi.org/10.1016/j.powtec.2014.01.001>.
- [40] A. Tamayol, M. Bahrami, Transverse permeability of fibrous porous media, *Phys. Rev. E* 83 (4) (2011) 046314, <http://dx.doi.org/10.1103/physreve.83.046314>.
- [41] D. Shou, J. Fan, F. Ding, Hydraulic permeability of fibrous porous media, *Int. J. Heat Mass Transfer* 54 (17–18) (2011) 4009–4018, <http://dx.doi.org/10.1016/j.ijheatmasstransfer.2011.04.022>.
- [42] K. Rezk, J. Forsberg, L. Nilsson, J. Berghel, Characterizing flow resistance in 3-dimensional disordered fibrous structures based on forchheimer coefficients for a wide range of Reynolds numbers, *Appl. Math. Model.* 40 (21–22) (2016) 8898–8911, <http://dx.doi.org/10.1016/j.apm.2016.05.036>.
- [43] Z. Wu, P. Mirbod, Experimental analysis of the flow near the boundary of random porous media, *Phys. Fluids* 30 (4) (2018) 047103, <http://dx.doi.org/10.1063/1.5021903>.
- [44] R. Rosenzweig, U. Shavit, The laminar flow field at the interface of a Sierpinski carpet configuration, *Water Resour. Res.* 43 (10) (2007) <http://dx.doi.org/10.1029/2006WR005801>, URL: <https://agupubs.onlinelibrary.wiley.com/doi/abs/10.1029/2006WR005801>.
- [45] M. Wang, N. Pan, Predictions of effective physical properties of complex multiphase materials, *Mater. Sci. Eng. R* 63 (1) (2008) 1–30, <http://dx.doi.org/10.1016/j.mser.2008.07.001>.
- [46] A. Sahu, S. Bhowmick, Applications of Lattice Boltzmann in method in multi-component and multi-phase flow: A review, *AIP Conf. Proc.* 2273 (1) (2020) 030007, <http://dx.doi.org/10.1063/5.0024322>.

- [47] G. Yang, Y. Chen, S. Chen, M. Wang, Implementation of a direct-addressing based lattice Boltzmann GPU solver for multiphase flow in porous media, *Comput. Phys. Comm.* 291 (2023) 108828, <http://dx.doi.org/10.1016/j.cpc.2023.108828>, URL: <https://www.sciencedirect.com/science/article/pii/S001046552300173X>.
- [48] K. Suga, Lattice Boltzmann methods for complex micro-flows: applicability and limitations for practical applications, *Fluid Dyn. Res.* 45 (3) (2013) 034501, <http://dx.doi.org/10.1088/0169-5983/45/3/034501>.
- [49] J. Wang, L. Chen, Q. Kang, S.S. Rahman, The lattice Boltzmann method for isothermal micro-gaseous flow and its application in shale gas flow: A review, *Int. J. Heat Mass Transfer* 95 (2016) 94–108, <http://dx.doi.org/10.1016/j.ijheatmasstransfer.2015.12.009>, URL: <https://www.sciencedirect.com/science/article/pii/S0017931015306566>.
- [50] Y. Kuwata, K. Suga, Lattice Boltzmann direct numerical simulation of interface turbulence over porous and rough walls, *Int. J. Heat Fluid Flow* 61 (2016) 145–157, <http://dx.doi.org/10.1016/j.ijheatfluidflow.2016.03.006>, URL: <https://www.sciencedirect.com/science/article/pii/S0142727X16300479>. SI TSFP9 special issue.
- [51] S. Khirevich, I. Ginzburg, U. Tallarek, Coarse- and fine-grid numerical behavior of MRT/TRT lattice-Boltzmann schemes in regular and random sphere packings, *J. Comput. Phys.* 281 (2015) 708–742, <http://dx.doi.org/10.1016/j.jcp.2014.10.038>, URL: <https://www.sciencedirect.com/science/article/pii/S0021999114007207>.
- [52] Q. Zou, X. He, On pressure and velocity boundary conditions for the lattice Boltzmann BGK model, *Phys. Fluids* 9 (6) (1997) 1591–1598, <http://dx.doi.org/10.1063/1.869307>.
- [53] J. Zhang, D.Y. Kwok, Pressure boundary condition of the lattice Boltzmann method for fully developed periodic flows, *Phys. Rev. E* 73 (4) (2006) 047702, <http://dx.doi.org/10.1103/physreve.73.047702>.
- [54] M. Hecht, J. Harting, Implementation of on-site velocity boundary conditions for D3Q19 lattice Boltzmann simulations, *J. Stat. Mech. Theory Exp.* 2010 (01) (2010) P01018, <http://dx.doi.org/10.1088/1742-5468/2010/01/p01018>.
- [55] M. Wang, N. Pan, Modeling and prediction of the effective thermal conductivity of random open-cell porous foams, *Int. J. Heat Mass Transfer* 51 (2008) 1325–1331.
- [56] Z. Wang, M. Wang, S. Chen, Coupling of high Knudsen number and non-ideal gas effects in microporous media, *J. Fluid Mech.* 840 (2018) 56–73, <http://dx.doi.org/10.1017/jfm.2018.46>.
- [57] G. Yang, M. Wang, Suitability of body force model for pressure-difference driven flow in porous media, *Comput. & Fluids* 265 (2023) 105990, <http://dx.doi.org/10.1016/j.compfluid.2023.105990>, URL: <https://www.sciencedirect.com/science/article/pii/S0045793023002153>.
- [58] T. Stylianopoulos, A. Yeckel, J.J. Derby, X.-J. Luo, M.S. Shephard, E.A. Sander, V.H. Barocas, Permeability calculations in three-dimensional isotropic and oriented fiber networks, *Phys. Fluids* 20 (12) (2008) 123601, <http://dx.doi.org/10.1063/1.3021477>.
- [59] M.F. Tachie, D.F. James, I.G. Currie, Velocity measurements of a shear flow penetrating a porous medium, *J. Fluid Mech.* 493 (2003) 319–343, <http://dx.doi.org/10.1017/S0022112003005986>.
- [60] M. Agelinchaab, M.F. Tachie, D.W. Ruth, Velocity measurement of flow through a model three-dimensional porous medium, *Phys. Fluids* 18 (1) (2006) 017105, <http://dx.doi.org/10.1063/1.2164847>.
- [61] M. Quintard, S. Whitaker, Transport in ordered and disordered porous media II: Generalized volume averaging, *Transp. Porous Media* 14 (2) (1994) 179–206, <http://dx.doi.org/10.1007/bf00615200>.